Astronomy
&
Astrophysics

Ice absorption features in the 5–8 μm region toward embedded protostars*

J. V. Keane[1], A. G. G. M. Tielens[1,2], A. C. A. Boogert[3], W. A. Schutte[4], and D. C. B. Whittet[5]

[1] Kapteyn Astronomical Institute, PO Box 800, 9700 AV Groningen, The Netherlands
[2] SRON, PO Box 800, 9700 AV Groningen, The Netherlands
[3] CalTech, Mail code 320-47, 1200 E. California Blvd., Pasadena, CA 91125, USA
[4] Leiden Observatory, PO Box 9513, 2300 RA Leiden, The Netherlands
[5] Department of Physics, Applied Physics & Astronomy, Rensselaer Polytechnic Institute, Troy, NY 12180, USA

Abstract. We have obtained 5–8 μm spectra towards 10 embedded protostars using the Short Wavelength Spectrometer on board the Infrared Space Observatory (ISO-SWS) with the aim of studying the composition of interstellar ices. The spectra are dominated by absorption bands at 6.0 μm and 6.85 μm. The observed peak positions, widths and relative intensities of these bands vary dramatically along the different lines of sight. On the basis of comparison with laboratory spectra, the bulk of the 6.0 μm absorption band is assigned to amorphous H_2O ice. Additional absorption, in this band, is seen toward 5 sources on the short wavelength wing, near 5.8 μm, and the long wavelength side near 6.2 μm. We attribute the short wavelength absorption to a combination of formic acid (HCOOH) and formaldehyde (H_2CO), while the long wavelength absorption has been assigned to the C–C stretching mode of aromatic structures. From an analysis of the 6.85 μm band, we conclude that this band is composed of two components: a volatile component centered near 6.75 μm and a more refractory component at 6.95 μm. From a comparison with various temperature tracers of the thermal history of interstellar ices, we conclude that the two 6.85 μm components are related through thermal processing. We explore several possible carriers of the 6.85 μm absorption band, but no satisfactory identification can be made at present. Finally, we discuss the possible implications for the origin and evolution of interstellar ices that arise from these new results.

Key words. ISM: dust, extinction – ISM: molecules – ISM: abundances – infrared: ISM – stars: formation

1. Introduction

Infrared spectroscopy has long been an important tool for the study of objects embedded in or located behind molecular clouds. Superimposed on the IR continua of many sources are absorption bands (Merrill et al. 1976; Willner et al. 1982) which, because of their widths, have been attributed to vibrational transitions of molecules in ices (Whittet 1993). Among the (simple) molecules that have been identified in interstellar grains are: H_2O, CO_2, CH_3OH, CO and CH_4, which are believed to be frozen onto the grain mantles (Whittet et al. 1996). A comparison of these spectral features, along different lines of sight, is a diagnostic of the evolutionary state of grain mantles.

The 5–8 μm region is of particular importance since

this region probes absorption bands of saturated hydrocarbons and carbonyls which are not as severely blended or influenced by strong absorption features, as in other spectral regions. Broad 6.0 μm and 6.85 μm absorption features dominate the 5–8 μm region and were previously investigated with the aid of low resolution airborne spectroscopy (Willner et al. 1982; Tielens et al. 1984; Tielens & Allamandola 1987; d'Hendecourt et al. 1996; Schutte et al. 1996). These results seemed to indicate that both features were nearly always constant in position and width. Furthermore, it appeared that the band intensities were relatively constant with respect to each other. The 6.0 μm band was assigned to absorption by H_2O ice, while the 6.85 μm band was attributed to CH_3OH (Tielens & Allamandola 1987). With the new high resolution observations of the Short Wavelength Spectrometer on board the Infrared Space Observatory (ISO-SWS) it is now possible to examine more closely the mid–infrared range.

The reduction procedures used to obtain the astronomical spectra are discussed in Sect. 2. In Sect. 3, we present the 5–8 μm spectra and analyse the spectral
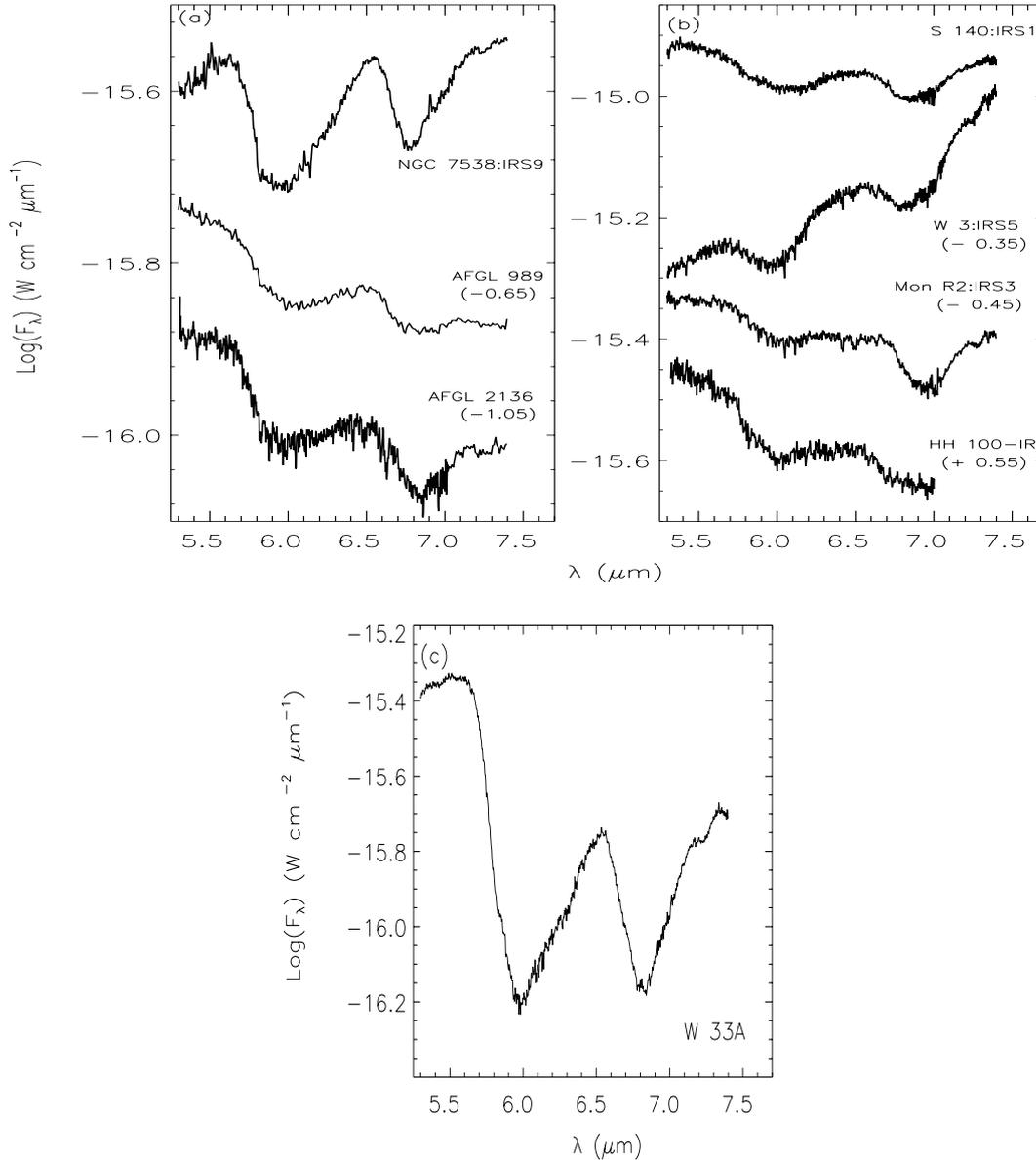
Fig. 1. ISO-SWS AOT6 observations of the 6.0 μm and 6.85 μm features towards different young stellar objects (YSO's). W33A had to be plotted separately **c)** in view of the strength of the ice features.

features. The identifications of the observed spectral features, and the comparisons with laboratory data, are discussed in Sects. 4 and 5. Finally, the evidence for thermal processing and the subsequent implications for the composition of interstellar ices are presented in Sect. 6.

2. Observations

The spectra were obtained with ISO-SWS. All but one of the sources, GL 989, were observed in the high resolution AOT6 mode ($\lambda/\Delta\lambda = 1600$). The source GL 989 was observed in the AOT1 fast scanning mode ($\lambda/\Delta\lambda = 400$). The data were reduced with the SWS Interactive Analysis package (de Graauw et al. 1996) using the latest version of the calibration files. Individual detector scans were checked for bad dark current subtraction and high noise

levels. Bad detectors were removed and the remaining detectors were checked for dark current jumps. The wavelength regions affected by these jumps were cut out of the data and the scans were flat-fielded to the rebinned down scan using a first order polynomial. Clipping all points that deviate by 3σ or more ensured that hits due to cosmic rays were also removed. In some sources, it was found that band overlaps did not match. To correct for this, band 2c ($7.0\ \mu m \leq \lambda \leq 12.0\ \mu m$) was shifted up or down in order to match the edge of band 2b at 7.0 μm. Comparison of the up and down scans revealed that there were no differences in the continuum slope or the profiles of the features. The reduced unsmoothed spectra are shown in Fig. 1. In addition to our sample, we have included the low mass object Elias 29 (Boogert et al. 2000b) and the high mass object GL 7009S (d'Hendecourt et al. 1996).

3. The continuum and absorption profiles

The spectra in Fig. 1 show, in all cases, the well known absorption features at 6.0 and 6.85 μm. In addition the spectra of W 33A, GL 2136, W3 IRS5 and Mon R2 IRS3 show weak absorption features at 7.25 and 7.41 μm; first discussed by Schutte et al. (1999) for the young stellar object W 33A. These will be further discussed in Keane et al. (in prep.). Also present in NGC 7538: IRS9 is an emission line due to the H_2 0–0, $S(5)$ transition. The presence of gas phase H_2O absorption lines between 5.5 and 6.6 μm toward some of the massive young stars in our sample has been well established (Helmich et al. 1996; van Dishoeck & Helmich 1996). Gas phase water lines are present in the spectra of GL 2136, W3 IRS5, Mon R2 IRS3 and HH 100 (Boonman et al. 2000).

3.1. Continuum determination

A local continuum was defined for the 5–8 micron region, fixed to the observed 5.3–5.6 μm flux. A modified black body ($\lambda^{-\beta}$), with $\beta = 1$, was adopted as the continuum fitted at 5.5 μm. As an example, Fig. 2a shows the adopted continuum for S140:IRS1. Anticipating our discussion in Sect. 4, the 6.0 μm band is largely due to H_2O ice. The dot-dashed line in Fig. 2a shows the corresponding laboratory H_2O feature. The water ice band extends well beyond the 6.85 μm feature. To accommodate this wing, we have adopted the dotted continuum in Fig. 2a. For comparison, we also consider a modified black body continuum fitted at 5.5 and 7.4 μm. The two profiles of the 6.0 and 6.85 μm absorption features derived from these two continua agree very well in position and profile (Fig. 2b). The two different continua only introduce slightly different total optical depths. This analysis has been applied to all the sources and no significant deviation in peak position or profile is found.

Peak positions, widths and optical depths for the features are summarized in Table 1. Given the "flatness" of the bottom of the absorption features, and the contamination by water lines a typical uncertainty of 12 cm^{-1} was determined on the peak position and *FWHM*. The error on the depth was determined from the noise seen in the bottom of the absorption features which results in a typical uncertainty of 0.1.

3.2. Absorption profiles

The continuum subtracted spectra are shown in Fig. 3. Two vertical lines are drawn to guide the eye at 6.0 μm and 6.85 μm, corresponding to the peak positions indicated by previous low resolution infrared spectroscopy of young stellar objects. As these higher resolution ISO observations make evident: previous peak position assignments are no longer applicable. We also emphasize that there are considerable differences in the strength and detailed shape of the absorption features.
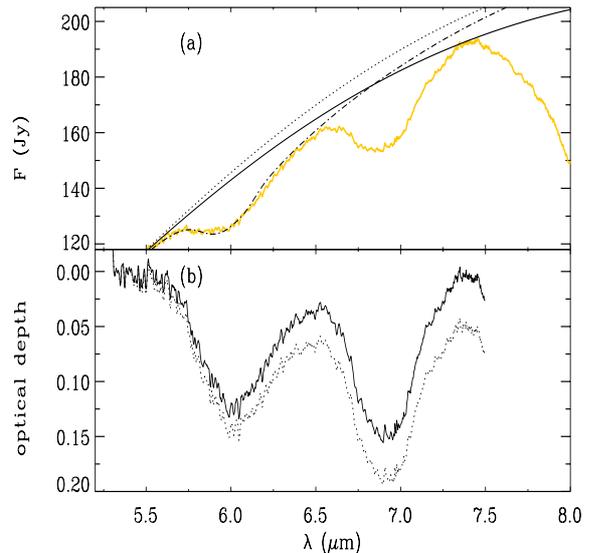

Fig. 2. Plot of two baseline extremes used to demonstrate the robustness of the peak position of the interstellar features. In the first panel **a)**, S140:IRS1 is shown with two different choices for continuum. The continuum subtracted profiles, in panel **b)**, show that there is no shift in peak position or variation in the shape of the profile.

3.2.1. 6.0 μm profiles

The 6.0 μm band profile, in particular its width, varies between the observed lines of sight (Fig. 3). The short wavelength side of the absorption band, in some sources, has a steeper slope where there appears to be an absorption shoulder near 5.8 μm, which is most notable in the spectra of NGC 7538:IRS9, W 33A, GL 989 and GL 7009S. There is also some evidence for a weak absorption feature near 6.25 μm, most notable in the spectrum of W33A.

3.2.2. 6.85 μm profiles

The 6.85 μm band profile varies remarkably in both peak position and profile between the observed lines of sight (Fig. 3). The 6.85 μm feature of NGC 7538:IRS9 peaks at the shortest wavelength position whereas the 6.85 μm band of Mon R2:IRS3 peaks at the longest wavelength position. Since it seems that the long wavelength wing of NGC 7538:IRS9 profile could be fitted by the Mon R2:IRS3 profile, we have subtracted the latter from NGC 7538:IRS9. For clarity this new profile is called component 1 and the Mon R2:IRS3 profile is called component 2. We hypothesize that the 6.85 μm band in all sources consists of a combination of these two components (Figs. 5 and 6). Table 2 summarizes the fraction of component 1 and component 2 fitted to all the sources. Thus we conclude that the interstellar 6.85 μm band observed in protostellar spectra likely consists of two components. Whether these components are chemically different or are essentially the same component which is being influenced by a different chemical or physical environment is discussed in Sect. 5.
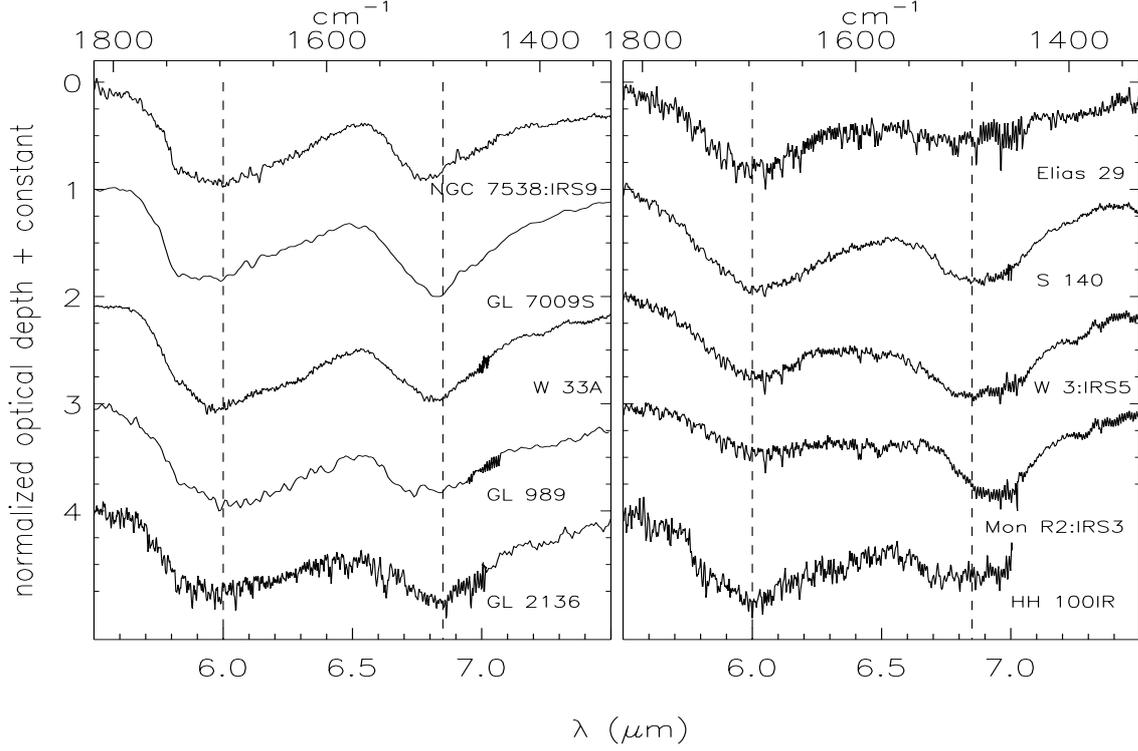
Fig. 3. Derived 6.0 μm and 6.85 μm optical depth profiles plotted in order of increasing wavelength shift seen in the 6.0 μm and 6.85 μm bands. The sources are all normalized to the depth of the strongest feature. The dashed vertical lines indicate the 6.0 μm and 6.85 μm positions.

Table 1. Observed spectral characteristics of features in the 5–8 μm region.

Parameter	NGC 7538 IRS9	GL 7009S[a]	W 33A	GL 989	GL 2136	Elias 29	S 140 IRS1	W 3 IRS5	Mon R2 IRS3	HH100	Units
ID tag[b]	1	2	3	4	5	6	7	8	9	10	
$\nu_{6.0}^{c}$	1666	1680	1684	1671	1700	1667	1652	1652	1652	1667	cm^{-1}
$\Delta\nu_{6.0}^{c}$	158	150	172	185	136	130	157	185	141	137	cm^{-1}
$\tau_{6.0}^{d}$	0.43	1.2	1.81	0.21	0.3	0.24	0.21	0.32	0.19	0.23	
$\nu_{6.85}^{c}$	1473	1462	1471	1471	1459	1470	1451	1459	1437	1470	cm^{-1}
$\Delta\nu_{6.85}^{c}$	83	85	79	88	69	91	92	98	71	—	cm^{-1}
$\tau_{6.85}^{d}$	0.29	1.1	0.78	0.11	0.23	0.07	0.13	0.25	0.23	0.09	
$\nu_{5.83}^{c}$	1718	1718	1721	1718	1715	—	—	—	—	—	cm^{-1}
$\Delta\nu_{5.83}^{c}$	30	47	30	32	47	—	—	—	—	—	cm^{-1}
$\tau_{5.83}^{d}$	0.15	0.54	0.34	0.03	0.08	—	—	—	—	—	
$\nu_{6.2}^{b}$	1597	1597	1589	1597	1605	—	—	—	—	—	cm^{-1}
$\Delta\nu_{6.2}^{c}$	60	58	65	65	34	—	—	—	—	—	cm^{-1}
$\tau_{6.2}^{d}$	0.07	0.14	0.32	0.03	0.03	—	—	—	—	—	

[a] Taken from d'Hendecourt et al. (1999); [b] A number assigned to the sources to help identify them in Fig. 8;
[c] The typical uncertainty is 12 cm^{-1}; [d] The typical uncertainty is 0.1.

4. The 6.0 μm feature

4.1. H$_2$O ice

The 6.0 μm band has long been assigned to the bending mode of amorphous H$_2$O ice (Tielens & Allamandola 1987), which is supported by the presence of the H$_2$O stretching mode at 3.1 μm. We first analyzed the 6.0 μm band by fitting laboratory spectra of pure amorphous H$_2$O ice, varying the ice temperature to optimize the fit (Fig. 4).

The temperatures of the ice bands that gave the best fits are shown in Table 2. All sources are fitted best by ices with temperatures $\leq$50 K, except for Mon R2:IRS3 which is well fitted by an 80 K ice. Since the laboratory spectrum of amorphous H$_2$O does not vary much upon warm-up to 50 K, it is very difficult to distinguish between the profile of a colder ice (10 K) and that of a warmer ice (50 K). The presence of warmed-up H$_2$O ice in space is well known from studies of the 3.1 μm H$_2$O band (Smith et al. 1989) and the derived temperatures agree well for those sources
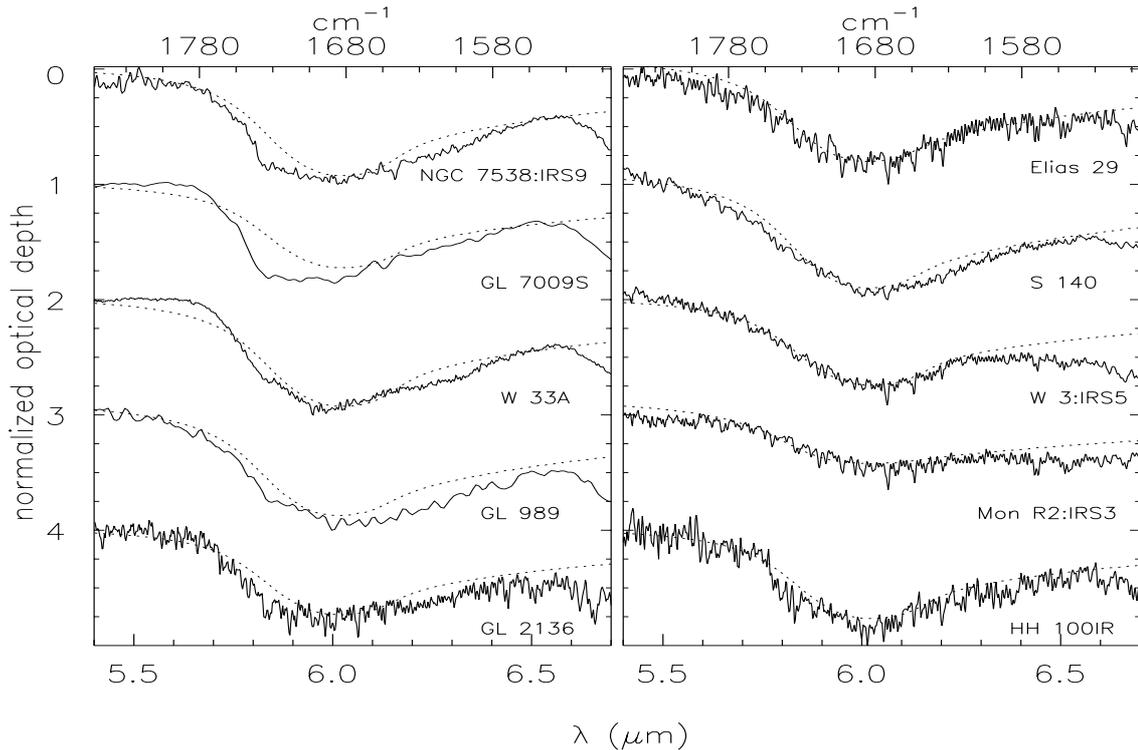
Fig. 4. Best fits for the interstellar 6.0 μm feature with solid H_2O laboratory ice (see text for temperature of fits).

in common between these two samples. Thermal processing of interstellar ice is also apparent from the profiles of the various solid CO_2 modes (Gerakines et al. 1999; Boogert 1999; Boogert et al. 2000a).

For 4 objects in our sample, good fits to the 6.0 μm band are obtained by fitting just amorphous H_2O ice (Elias 29, W 3:IRS5, Mon R2:IRS3 & HH 100). For the remaining sources, (NGC 7538:IRS9, W 33A, GL 989, GL 2136 & S 140:IRS1), subtracting H_2O ice from the 6.0 μm band reveals at least two additional components absorbing in this region (Fig. 4). The excess absorptions are centered at 5.83 μm and 6.2 μm (cf. Fig. 10 and Sects. 4.3 and 4.4).

In the case of W 33A, and to a lesser extent GL 7009S, the H_2O ice fit to the edge of the blue wing of the 6.0 μm band is very poor. There are two possible ways to account for this: 1) the adopted continuum is incorrect, or 2) the 6.0 μm band in these two sources is mainly due to an unknown absorber. Addressing the first possibility, adopting the laboratory H_2O ice spectrum we derive the continuum shown for W 33A in Fig. 7a (dotted line). Compared to the original continuum, there is a curious break shortwards of 5.5 μm. Of course, one might presume the presence of a weak absorber peaking at a shorter wavelength but the full SWS spectrum of this source shows no indication for this (Gibb et al. 2000). As to the second possibility, we have subtracted the maximum amount of H_2O ice possible (determined from the 3.1 μm ice band; Fig. 7c solid line) and the residual absorption is shown, for W 33A, in Fig. 7d (solid line). A substantial part of the 6.0 μm feature is then due to an unknown ice compound

that happens to absorb at exactly the same peak position and with the same width as H_2O ice. Moreover, there is no evidence for any other strong absorption features due to this species in the mid-IR range. Neither of the two solutions is very satisfactory and detailed radiative transfer studies may help to elucidate the continuum uncertainty.

An additional problem is that the H_2O column density derived from the 3.1 μm band is much less than that derived from the 6.0 μm band (Gibb et al. 2000). While not as extreme in other sources, this discrepancy between the 6.0 and the 3.1 μm H_2O column densities seems to be a general problem. Figure 8a compares the optical depths of the 3.1 μm and 6.0 μm bands with laboratory measurements of their relative strengths. All sources fall above the line in Fig. 8a, indicating that either the depth of the 3.1 μm feature or the depth of the 6.0 μm band is incorrect. Part of this discrepancy may reflect the problem of the long wavelength wing in the 3.1 μm feature which cannot be fitted by absorption due to small ($\leq$0.3 μm) amorphous H_2O ice (Hagen et al. 1981). The additional absorption has been alternatively attributed to the C–H stretching vibration of hydrocarbons, to extinction by large H_2O ice grains and to absorption by H_2O hydrogen bonded to strong bases, such as NH_3, (Hagen et al. 1981; Léger et al. 1983; Tielens & Allamandola 1987; Sellgren et al. 1994). If we attribute the long wavelength wing to absorption by H_2O, the integrated strength of the 3.1 μm band is increased by about 40%. Figure 8b plots the 6.0 μm optical depths as a function of the calculated integrated area for the 3.1 μm band (defined from 2.7 μm to 3.7 μm). The solid line is the relationship
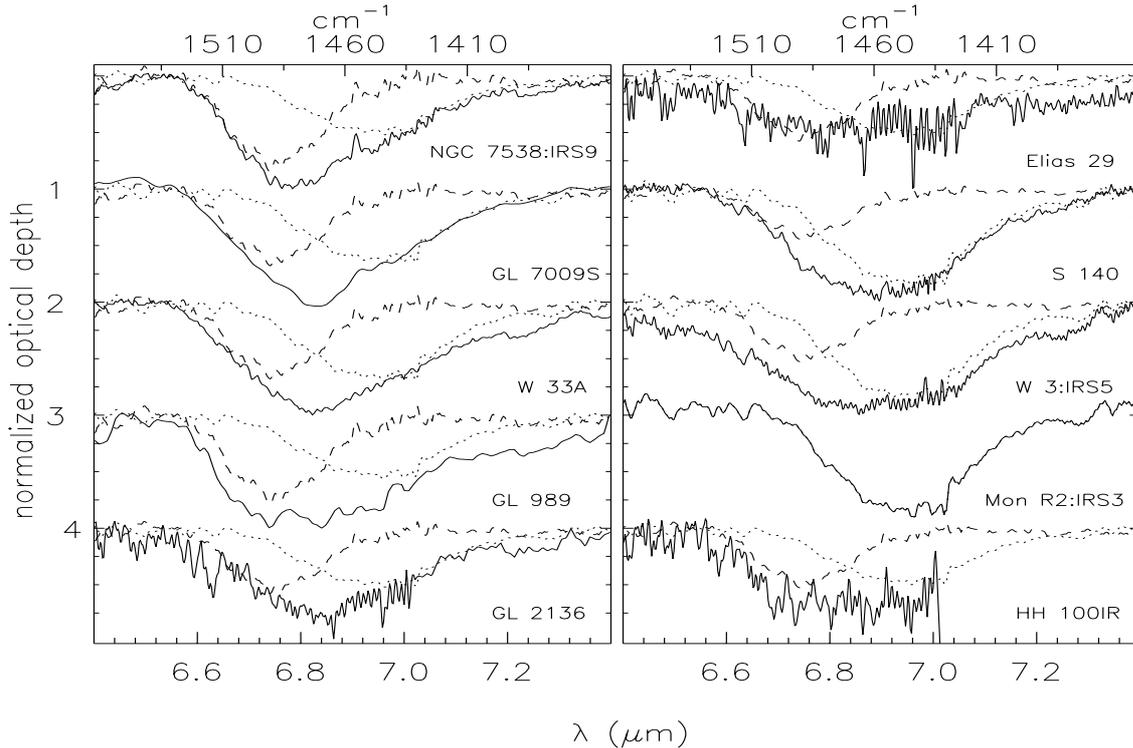
Fig. 5. A plot of the amount of component 1 (dashed line) and component 2 (dotted line) contributing to each of the 6.85 μm feature (see Table 2 for the ratio of component 1 to component 2).

between the integrated area of the 3.1 μm band and the optical depth of the 6.0 μm band measured for H_2O ice in the laboratory. This procedure improves the fit of the experimental data to the observations (Fig. 8b), suggesting that indeed the long wavelength wing may be due to absorption by H_2O ice. The source W33A remains however an enigma.

For W33A, additional constraints on the column density can be gleaned from the H_2O $3\nu_L$ combination mode, which extends from 3.7 μm to 5 μm (Gibb et al. 2000). The H_2O column density, for this band, agrees well with the column density derived from the 3.1 μm H_2O band rather than the 6.0 μm H_2O feature. This discrepancy between the H_2O column densities derived for W33A from the 3.1 μm and 6.0 μm band has been noted before (Tielens & Allamandola 1987) and ascribed to the presence of a reflection nebula associated with the disk geometry around the protostar (Pendleton et al. 1990). In this way, near-IR photons may preferentially scatter through the poles suffering relatively little extinction, while the mid-IR photons follow a more extinguished direct path. As a result, column densities derived from long wavelength features might be augmented relative to those derived from features at shorter wavelengths. Evidence of such a scenario should also be found in other absorption features which fall within the same wavelength range as the H_2O features (see Sect. 5.1.2), but the CO_2 bands at 4.27 μm and 15.2 μm do not lend support to this scenario as the column densities derived from these features are very consistent.

Summarizing: Overall, H_2O ice provides a good fit to the observed 6.0 μm band and the 6.0 μm H_2O column densities were determined by assuming that H_2O ice is the dominant carrier of this band (see Table 2).

4.2. NH$_3$ ice absorption

The presence of solid state NH_3 has in general been very difficult to establish since the main vibrational bands blend with the H_2O and silicate bands. Recently, Lacy et al. (1998) identified a feature at 9 μm (1110 cm^{-1}), in the spectrum of NGC 7538:IRS9, with the strong inversion mode of NH_3. New detections of NH_3 ice have also been reported by Chiar et al. (2000) toward the Galactic Center (stretching mode) and by Gibb et al. (2000) toward W33A (inversion mode). The spectral presence of NH_3 ice in other regions of the spectrum implies that there must also be NH_3 absorption (NH-deformation mode) at 6.15 μm contributing to the 6.0 μm feature.

Comparison of the 9 μm inversion mode with various laboratory profiles indicate that the NH_3 is most likely frozen in an H_2O-rich ice (Lacy et al. 1998; Gibb et al. 2000). The measured column density of NH_3 toward NGC 7538:IRS9 is 9.3×10^{17} cm^{-2} (Lacy et al. 1998) and 1.7×10^{18} cm^{-2} toward W33A (Gibb et al. 2000). Examination of various H_2O:NH_3 laboratory mixtures reveals that the maximum amount of NH_3 that can be present without altering the profile of the 6.0 μm H_2O band is $\sim$9% relative to H_2O. As the amount of NH_3 is increased, the 6.0 μm profile shifts to longer wavelengths as a consequence of the NH_3 feature protruding from the
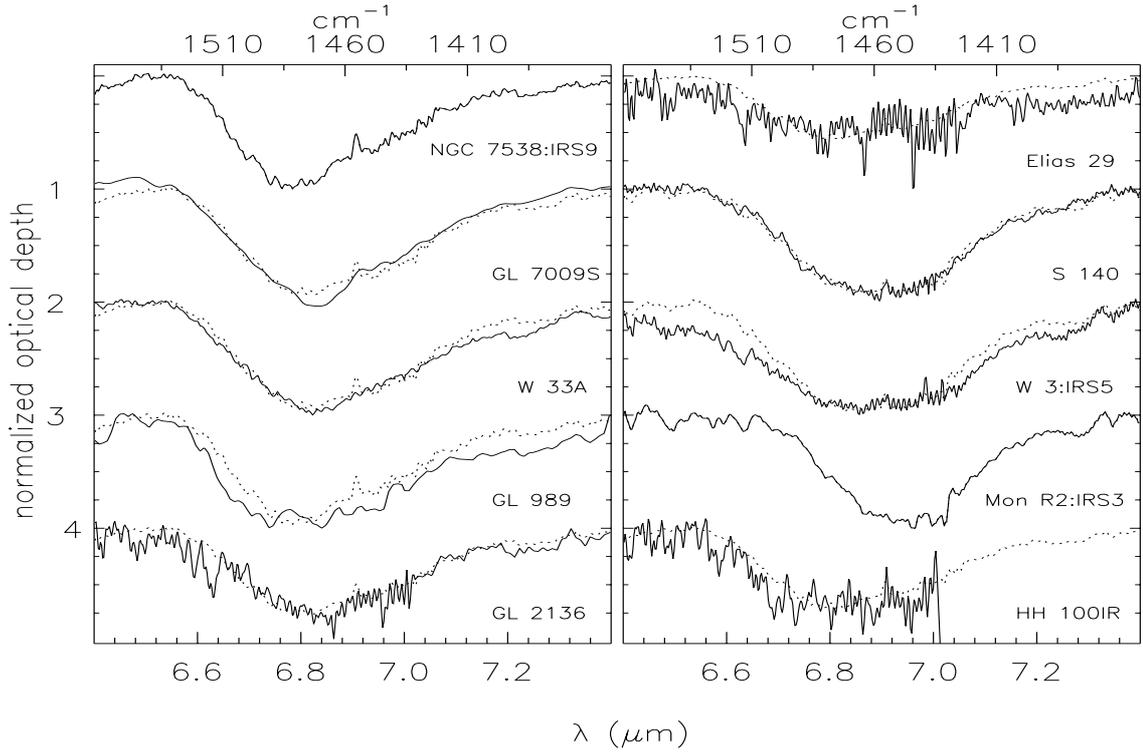
Fig. 6. A comparison of the 6.85 μm feature to the fit achieved by combining the component 1 and 2 profiles.
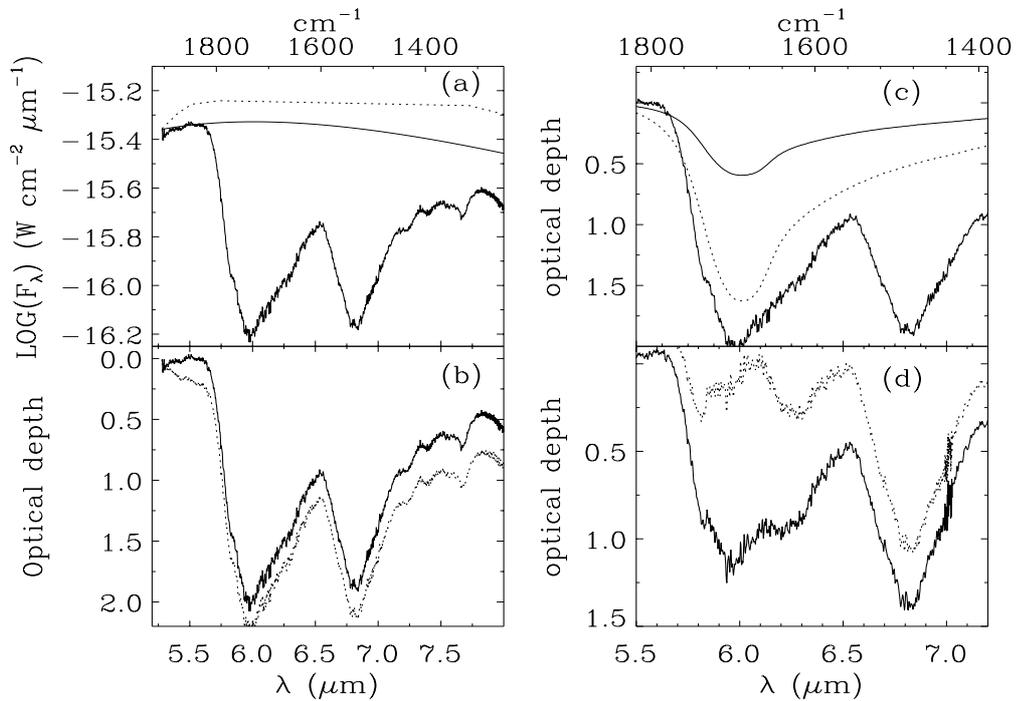

Fig. 7. Plot **a)** shows the continuum (solid line) chosen for W33A along with the unusual continuum (dotted line) which seemed necessary to fit the 6.0 μm band. The additional absorption near 5.5 μm that results from this unusual continuum (dotted line) is shown along with the profile determined from the adopted continuum (solid line) in plot **b)**. Plot **c)** shows the depth of the H_2O fit as determined from the column of H_2O ice in the 3.1 μm interstellar ice band (solid line), and if determined from the depth of the 6.0 μm interstellar band (dotted line). The H_2O subtracted profiles are shown in plot **d)**, illustrating the substantial absorption from components other than H_2O if the 3.1 μm ice band column density is used (solid line).
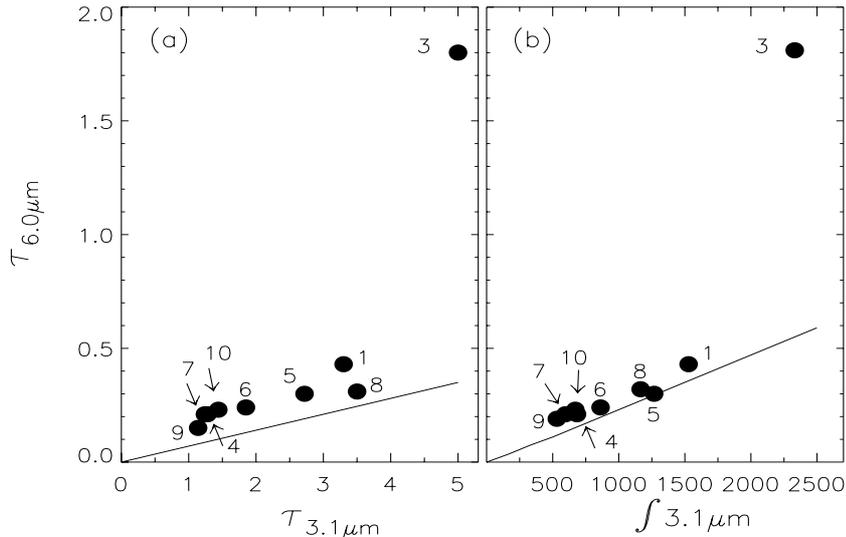
Fig. 8. 6.0 μm feature optical depths versus 3.1 μm optical depths and integrated areas of the 3.1 μm band. To match a source with its corresponding number see Table 1. GL 7009S, source 2, was not plotted as there is high extinction at 3.1 μm. The left panel **a)**, plots 6.0 μm feature optical depths (determined from this work) vs. 3.1 μm optical depths (taken from the literature). The solid line represents the expected optical depths for the 3.1 μm and 6.0 μm bands, as calculated from a laboratory H_2O ice sample at 10 K. See text for explanation of difference between predicted and observed optical depths. The right panel **b)**, attempts to correct for the deviation seen in the left panel. In this case the integrated area for the 3.1 μm feature, including the long wavelength wing (see text), is plotted against the 6.0 μm optical depth. The solid line represents the expected integrated 3.1 μm area and 6.0 μm optical depth for a given 3.1 μm optical depth.

bottom of the water band at 6.14 μm (Fig. 9). This upper limit to the NH_3 abundance can be expressed in terms of column density: 9×10^{17} cm^{-2} and 3.6×10^{18} cm^{-2} respectively, which are consistent with the recent observations of the 9.1 μm NH_3 features.

4.3. The 5.8 μm absorption

Examining the spectra, we note that the excess absorption centered at 5.83 μm (1715 cm^{-1}) may actually consist of two components: a narrow (0.05 μm) feature at 5.81 μm superimposed on a broader (0.2 μm) component at about 5.83 μm (Fig. 10). Absorption in this wavelength range is characteristic of the C=O stretching mode of carbonyl groups. Ketones, aldehydes, carboxylic acids, and esters all show a strong carbonyl stretch between 1870 cm^{-1} and 1700 cm^{-1}. For each of these classes of molecules the range in absorption frequency of the carbonyl stretch is actually much less. Electro-negative groups or atoms attached to the alcoholic oxygen tend to increase the frequency of the C=O stretching vibration.

4.3.1. HCOOH

While HCOOH was originally considered as a candidate for the full 5.8 μm feature, here we only attribute the underlying broad component to HCOOH. Figure 10 shows a comparison between the 5.8 μm absorption and the C=O stretching mode of HCOOH. Assuming a band strength of 6.7×10^{-17} cm/molecule for the C=O stretching mode (Maréchal 1987), the abundance of HCOOH determined is shown in Table 2. We emphasize that HCOOH has a very

extended red wing, which prevents a good fit to the narrow component of the 5.83 μm absorption feature.

HCOOH also has strong absorption bands at 3.06 μm and 8.2 μm, however these are blended with the H_2O and silicate bands respectively. Another HCOOH band is expected near 7.25 μm, and indeed a weak feature near 7.24 μm has been detected in some of the sources (Keane et al. in prep.). It has been proposed that the 7.24 μm absorption, in W33A, is well matched by the CH deformation mode of HCOOH (Schutte et al. 1999). However, sources which show no evidence for 5.8 μm absorption (e.g. Mon R2:IRS3) do display a prominent absorption feature near 7.24 μm (Keane et al. in prep.).

4.3.2. H_2CO and other candidates

Formaldehyde is a good candidate for the narrow 5.81 μm component (d'Hendecourt et al. 1996). Aldehydes, ketones and saturated aliphatic esters all absorb at 5.7–5.9 μm. Ketones and esters tend to have peak a position that is blue of the interstellar 5.8 μm feature. Figure 10 compares a laboratory spectrum of pure H_2CO at 10 K to the 5.8 μm interstellar absorption feature. The H_2CO profile is considerably wider than the observed feature. However, substituting H_2CO into a H_2O dominated mixture results in a narrowing of the laboratory feature (Schutte et al. 1993).

The H_2CO column density was determined from the observed integrated, narrow 5.81 μm band using the laboratory integrated strength of pure H_2CO which is not affected by substitution ($A_{H_2CO} = 9.6 \times 10^{-18}$ cm/molecule;

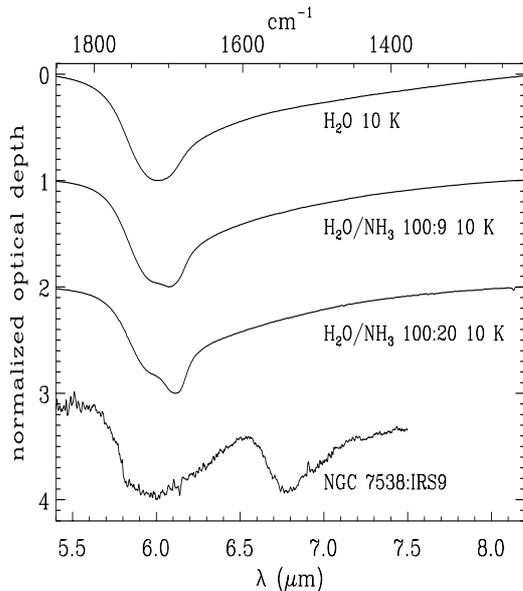**Fig. 9.** Laboratory profiles of pure H_2O ice and H_2O/NH_3 mixtures compared to the interstellar 6.0 μm band of NGC 7538:IRS9. As the amount of NH_3 in the mixtures is increased, the profile of the H_2O band begins to change, resulting in a protruding feature near 6.14 μm associated with NH_3. Increasing the NH_3 abundance, relative to the H_2O ice, results in the distortion of the smooth 6.0 μm H_2O ice band, which is not seen in the interstellar source.

Fig. 10. Comparison of the 6.0 μm band residuals with possible candidates. The top two panels are possible candidates for the 5.8 μm absorption feature. All laboratory profiles are at 10 K. The WR 118 profile is representative of the 6.2 μm absorption feature in the diffuse ISM and the dotted line is the continuum (Schutte et al. 1998; Chiar et al. 2000).

Schutte et al. 1993; see Table 2). Besides the 5.8 μm band, which is the strongest band, H_2CO has a feature at 6.68 μm with a strength roughly a third of the strength of the carbonyl mode. This feature is difficult to find due to its proximity to the 6.85 μm absorption band. H_2CO has been tentatively identified through a very weak feature at 3.47 μm (C–H stretch) in W 33A (Brooke et al. 1999) and GL 2136 (Schutte et al. 1996). Our estimates of the H_2CO column densities are in agreement with these studies. All other H_2CO bands are considerably weaker and would pose quite a challenge to try and identify them.

4.4. The 6.2 μm PAH absorption?

In the massive protostars, the peak position of the red excess is centered at 6.24 μm (1602 cm^{-1}) and this is characteristic of the C–C stretching modes of aromatic structures. Schutte et al. (1996) proposed that the 6.2 μm feature may be the absorption counterpart of the well known 6.2 μm PAH emission feature. The nature of the carrier imposes restrictions on the carbon abundance required to reproduce the strength of the interstellar 6.2 μm feature. Adopting the intrinsic strength for neutral PAHs, the fraction of the elemental carbon locked up in PAHs is calculated to be about 83% for NGC 7539:IRS9.

However, the intrinsic strength of this band is very sensitive to the degree of ionization (Langhoff 1996; Hudgins & Allamandola 1995). The charge due to cosmic ray ionization of the gas will be transferred through charge exchange or proton transfer reactions to the PAHs. This may
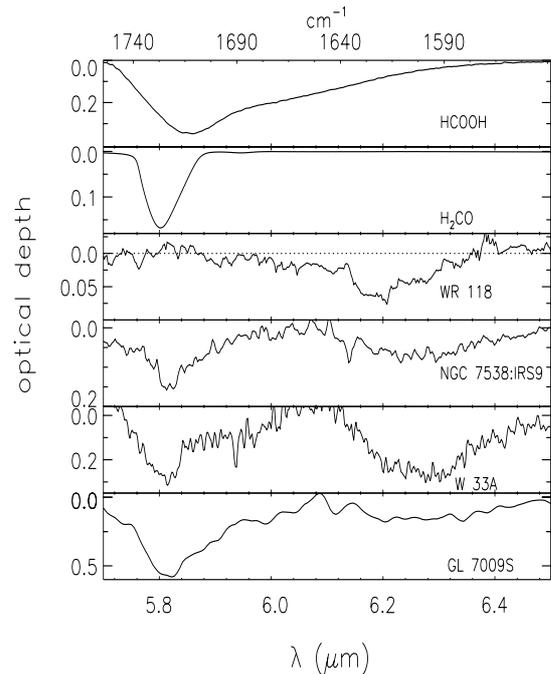
keep a substantial fraction of the PAHs ionized (Lepp & Dalgarno 1988) and the fraction of carbon in PAHs is then only 20 ppm relative to H (7% of the elemental C), a very reasonable amount given observations of the UIR bands (Tielens et al. 1999). Note, however, that this implicitly assumes that PAHs remain in the gas phase and do not freeze out in the ice mantles.

The 6.2 μm band might, in principle, also be due to carbonaceous dust. In the case of Hydrogenated Amorphous Carbon (HAC), formed from the burning of benzene (Colangeli et al. 1995), the strongest absorption band still requires an amount of carbon 100 ppm relative to H (35% of the elemental C) to be locked up in HACs, which though not unreasonable is more than that required for gaseous PAHs.

The profile of the 6.2 μm absorption feature toward the YSO's differs somewhat from the diffuse medium 6.2 μm absorption feature (WR 118 in Fig. 10), which has also been tentatively identified with PAH absorption (Schutte et al. 1998; Chiar et al. 2000). The 6.2 μm feature toward embedded objects is generally broader, smoother in appearance with a peak position slightly to the red of the diffuse feature which shows a pronounced peak at 6.18 μm. An absorption feature at 3.25 μm, which is tentatively attributed to absorption by gas phase PAH molecules, was first detected in spectra of Mon R2:IRS3 (Sellgren et al. 1994, 1995), and later detected towards S 140:IRS1 (Brooke et al. 1996). These are precisely the sources for which we do not observe a 6.2 μm band.

Likewise, sources with clear 6.2 μm bands, such as W 33A and NGC 7538:IRS9, do not show the 3.25 μm band. While this may reflect a difference in the degree of ionization – PAH cations have a weak 3.3 μm feature while neutral PAHs have a weak 6.2 μm band –, it sheds some doubt on this proposed identification.

Nevertheless, we deem the identification of the 6.2 μm band, seen toward molecular clouds, with the C–C stretch of aromatic structures as credible, since the abundance constraints for carbon can be well met.

5. Analysis of the 6.85 μm feature

As discussed in Sect. 3.2.2, all observed 6.85 μm features can be well fitted by 2 components. Figure 5 shows the separate components contributing to each observed 6.85 μm feature, while Fig. 6 compares the fit to the observed profile. A realistic candidate (or candidates) must account for the shift in position between the sources and the apparent lack of substructure within the 6.85 μm absorption feature.

5.1. Hydrocarbons

The 5–8 μm region is dominated by the CH, OH, and NH deformation modes and the C=O stretching mode. The 6.85 μm feature falls at the correct frequency for identification with the deformation modes in saturated hydrocarbons (Hagen et al. 1980; Tielens & Allamandola 1987).

5.1.1. Aliphatic hydrocarbons

Simple saturated aliphatic hydrocarbons, such as methyl (–CH$_3$–) and methylene (–CH$_2$–) groups, give rise to an asymmetric deformation band occurring at 6.76–6.94 μm, which in the presence of adjacent unsaturated groups shifts beyond 6.94 μm. The absorption profile of these bands, in alkanes (C$_n$H$_{2n+2}$), are too narrow to account for the interstellar 6.85 μm feature. Furthermore, if the 6.85 μm band was a result of the combination of saturated and unsaturated –CH$_3$–/–CH$_2$– modes then some substructure is expected in the feature. Furthermore, an assignment with saturated aliphatic hydrocarbons would imply the presence of strong –CH$_3$–/–CH$_2$– stretching modes near 3.4 μm, contrary to the observations which are consistent with at most a very weak 3.4 μm band, lost in the 3.1 μm wing. Thus, saturated aliphatic hydrocarbons are not a major component of the 6.85 μm feature.

5.1.2. Methanol and alcohols

The alcoholic OH group, which is electro-negative, coupled with the CH deformation mode produces an absorption that is much broader than the saturated aliphatic features. Based upon comparison of low resolution spectra with laboratory ice samples containing methanol, CH$_3$OH has been proposed as the carrier for the 6.85 μm feature (Tielens & Allamandola 1987). The presence of CH$_3$OH
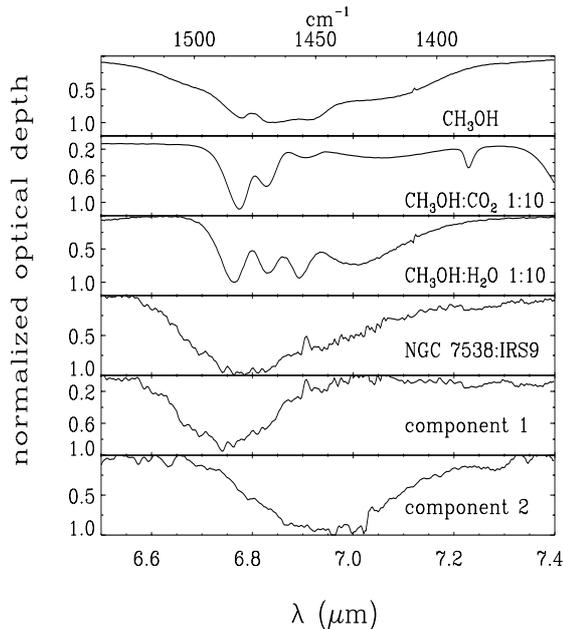

Fig. 11. A comparison of the 6.85 μm feature (components 1 and 2) with the deformation mode of solid CH$_3$OH mixtures at 10 K. The triple peak structure of CH$_3$OH is more pronounced in an H$_2$O mixture, while the substructure for pure CH$_3$OH becomes smoothed. The complete 6.85 μm band of NGC 7538:IRS9 is also shown, for comparison with pure CH$_3$OH which has minimal substructure but is broader than the interstellar feature.

was confirmed, to some extent (but see below), by the detection of the CH$_3$OH stretching mode at 3.54 μm (Grim et al. 1991; Allamandola et al. 1992). Also, detailed fits to the interstellar CO$_2$ stretching and bending modes reveals the presence of CH$_3$OH ice mixed in with the CO$_2$ (Gerakines et al. 1999; Boogert 1999). However, Grim et al. (1991) pointed out that the CH$_3$OH column densities derived from the 3.54 and the 6.85 μm bands were inconsistent. Furthermore, the recent high resolution ISO observations have revealed additional serious failings with the CH$_3$OH assignment to the 6.85 μm band. In no specific order they are, incorrect peak position, lack of substructure, and finally a column density discrepancy.

The problems associated with incorrect peak position and lack of substructure are intimately coupled with the composition of the ice mixture. As shown by Schutte et al. (1996) for NGC 7538:IRS9, a comparison of the 6.85 μm feature with a composite spectrum of H$_2$O:HCOOH:CH$_3$OH highlights that the methanol feature falls somewhat red of the interstellar feature. Furthermore, upon warmup the band position remains very stable. Figure 11 summarizes the peak positions of the CH$_3$OH deformation mode in various ice mixtures. In the case of component 1, CH$_3$OH is consistently at too long a wavelength, whereas, component 2 is at slightly longer wavelengths than the CH$_3$OH profiles. The degree of substructure observed in the laboratory profiles is also quite considerable, whereas the interstellar profiles show very little evidence for substructure. The degree of
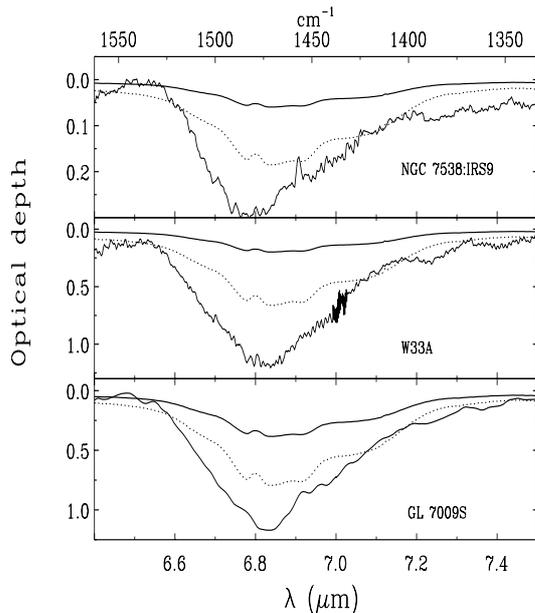
Fig. 12. The interstellar 6.85 μm feature compared to solid CH$_3$OH at 10 K, using the 3.54 μm CH$_3$OH band as an estimate for the amount of CH$_3$OH that can contribute to this band. The solid line is the column density of CH$_3$OH as determined from the 3.54 μm CH$_3$OH band, while the dotted line is the maximum about of CH$_3$OH that can be fitted to the interstellar 6.85 μm band.

substructure, however, is very sensitive to the matrix composition (Fig. 11). A pure CH$_3$OH laboratory sample displays a fairly smooth profile. However, upon increasing the amount of H$_2$O or CO$_2$, substructure within the band begins to appear. This substructure is usually characterized by three narrow peaks and a broad shoulder. The broad shoulder of CH$_3$OH makes its profile much broader than either of the interstellar components. In particular, component 1 shows very little evidence of a wing on the long wavelength side. The shoulder diminishes in strength when CH$_3$OH is placed in a CO$_2$ rich matrix but there is then a very pronounced double peak structure to the band. A powerful constraint on the matrix composition can be gleaned from the CO$_2$ bending mode seen toward embedded objects. This feature is very sensitive to ice composition and temperature (Gerakines et al. 1999; Boogert 1999) and can only be fitted by specific laboratory mixtures. It is evident from fitting laboratory profiles to the CO$_2$ bending mode that in addition to CH$_3$OH, a substantial amount of H$_2$O must be present. The inclusion of H$_2$O ice implies that there will always be a very pronounced triple peak profile to the CH$_3$OH deformation band. In principle, many different ice compositions might be present along the line of sight, so that the observed feature may therefore be a superposition of many different profiles, either pure or mixed mixtures. However, the addition of many different CH$_3$OH laboratory profiles at various temperatures failed to produce a smooth profile similar to the interstellar 6.85 μm band.

The abundance discrepancy has been highlighted for sometime (Grim et al. 1991). Assuming that the 6.85 μm band is due solely to CH$_3$OH, the column density that is derived is significantly higher than what is derived from the CH$_3$OH stretching mode at 3.54 μm. Adopting the column densities derived from the 3.54 μm feature, it is very obvious that, in the majority of cases, CH$_3$OH can contribute at most 10% to the 6.85 μm band (Fig. 12), an exception being GL 7009S, where 30% of the feature may be due to CH$_3$OH (Dartois et al. 1999). In a way, this may be the same problem as seen for the 3.1 μm and 6.0 μm H$_2$O bands and discussed in Sect. 4. CH$_3$OH column densities have not been determined due to the lack of support for a CH$_3$OH assignment to the 6.85 μm feature.

In summary, though CH$_3$OH is present in this band there are many reasons not to assign this as the dominant 6.85 μm carrier. The most obvious problem is that laboratory CH$_3$OH profiles peak at a different wavelength and have significant amounts of substructure whereas in comparison the interstellar feature is very smooth.

5.1.3. The effect of carbonyl and nitrile groups

If electro-negative groups are attached to hydrocarbon chains, the intensity of the stretching mode at 3.4 μm decreases while the deformation mode at 6.85 μm becomes stronger (Wexler 1967). When an unsaturated group, such as a carbonyl group (C=O), is adjacent, the bending intensities are increased approximately 10 times in the 6.8–7.3 μm region,while the stretching intensities are reduced by a similar factor (Wexler 1967; d'Hendecourt & Allamandola 1986). The same effect is also observed if nitrile groups (C≡N) are attached, with no apparent shift in position of the bending and stretching modes. Though it may be possible to account for the weakness of the 3.4 μm hydrocarbon band, new absorption bands arise from the attachment of electro-negative groups. If C=O groups are attached, a very strong CO stretch is expected near 5.75 μm with an intensity approximately 5 times greater than the deformation mode. Also, if C≡N groups are attached, absorption is expected between 4.37 μm and 4.44 μm. Neither the C=O or C≡N is seen in the interstellar spectra. Furthermore, the band intensity of the CH deformation mode near 7.3 μm will also increase in strength, paralleling the 6.85 μm band. Though an absorption feature is observed in all sources near 7.3 μm, its strength is inconsistent with that expected from attaching electro-negative groups.

5.2. NH$_4^+$

An identification with the NH$_4^+$ ion was proposed by Grim et al. (1989). The NH$_4^+$ ion is produced by UV photolysis of specific ices containing H$_2$O, CO and NH$_3$. However, the photolysed mixture had to be heated to a specific temperature in order to shift the ion band to the appropriate interstellar position. NH$_4^+$ can also be produced by the
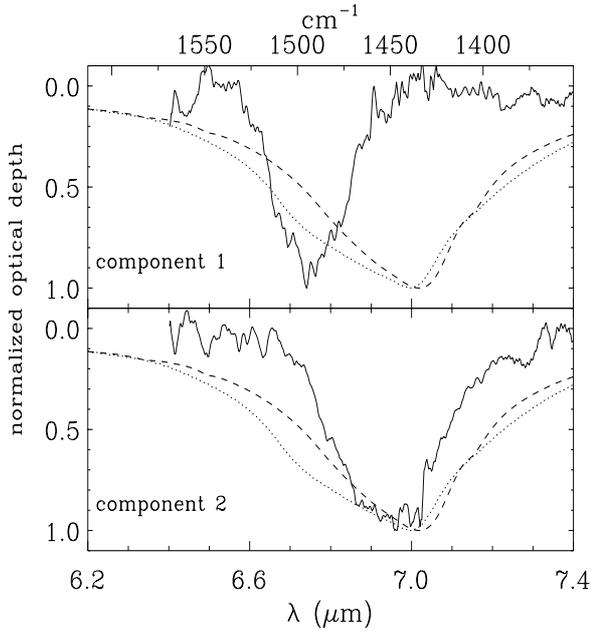
Fig. 13. A comparison of the 6.85 μm feature (components 1 and 2) with carbonates. The dotted line (...) is dolomite (CaMgCO$_3$) and the dashed line (- - -) is calcite (CaCO$_3$).

simple acid base reaction: HNCO + NH$_3$ $\longrightarrow$ OCN$^-$ + NH$_4^+$ (Keane 1997; Keane et al. in prep.). The band position of the ion is sensitive to temperature and hence it may account for the observed shift in peak position. However, an exclusive assignment of NH$_4^+$ to the 6.85 μm feature would imply significant absorptions due to counter-ions. A feature at 4.62 μm (Schutte & Greenberg 1996) has been tentatively identified as absorption by a negative ion, OCN$^-$. If the absorption at 6.85 μm is due to NH$_4^+$ then a correlation with the 4.62 μm feature would be expected. There is no evidence for such a correlation. In particular, some sources that have a very prominent 6.85 μm absorption feature do not display absorption at 4.62 μm, (e.g. Mon R2:IRS3). Thus, NH$_4^+$ is not a major component of the 6.85 μm feature because of the spectral mismatch and in view of the absence of sufficient counter ions.

5.3. Carbonates

Infrared spectra of interplanetary dust particles, IDPs, have shown the presence of absorption features near 7.0 μm and 11.4 μm which are characteristic of carbonates and it has been proposed that carbonates are likely candidates for the interstellar 6.85 μm feature as well (Sandford & Walker 1985; Hecht et al. 1986). The IDP carbonates are probably due to reactions of CO$_2$ with hydrated magnesium or calcium in an aqueous (planetismal) environment (Huang & Kerr 1960). The peak-position of this carbonate band is sensitive to particle size and shape (Huffman 1977) and therefore might account for the wavelength shifts of this band seen in our sample. However, the carbonate profile is considerably broader than both components of the interstellar 6.85 μm (Fig. 13). If carbonates are present,

then associated with the 7.0 μm peak are weaker features at 11.4 μm and 27 μm. If the 7.0 μm feature has an optical depth of τ, then the 11.4 μm and 27 μm features are expected to have optical depths of $\tau/4$ and $\tau/3$, respectively. The 6.85 μm band of W33A has an optical depth of 0.78, therefore the 11.4 μm feature is required to have a depth of 0.15. Though the search for the 11.4 μm feature is made difficult by strong interstellar silicate absorption at 10 μm, the carbonate feature should be seen as a narrow absorption profile superimposed in the silicate feature and is not. Hence, carbonates are not a realistic choice for the 6.85 μm feature.

5.4. Summary of proposed 6.85 μm carriers

The carrier(s) responsible for the interstellar 6.85 μm band has not been conclusively identified. A successful candidate must account for three stringent observational criteria – 1) shift in position, 2) lack of substructure, 3) be abundant –, and none of the proposed candidates match all three requirements. Furthermore, the two components of the 6.85 μm band (NGC 7538:IRS1 and Mon R2:IRS3) are poorly matched by any of the suggested candidates. Even if the interstellar 6.85 μm band is considered as a single component, this still does not help to elucidate the carrier. Small contributions to the 6.85 μm feature can be attributed to CH$_3$OH and NH$_4^+$. However, neither of these molecules can account for the bulk of the 6.85 μm band, either because of abundance constraints or due to the lack of sufficient counter-ions. The remaining proposed 6.85 μm carriers (e.g. carbonates) are not viable candidates as their profiles never approximate the observed interstellar feature.

6. Discussion

6.1. Evidence for thermal processing of ices

The importance of thermal processing for the evolution of interstellar ices is now well established. The effect of thermal processing is particularly evidenced in the profiles of the ^{12}CO$_2$ and ^{13}CO$_2$ absorption bands (Gerakines et al. 1999; Boogert 1999; Boogert et al. 2000a, 2000b). Comparison of the band profiles toward massive hot cores revealed double peaked structure within the ^{13}CO$_2$ stretching and ^{12}CO$_2$ bending modes, most likely caused by the heating of polar ices. While not as sensitive, the observed profile of the 3.1 μm and 6.0 μm H$_2$O ice bands is also a trace of heating of interstellar ices. To establish that there is, in fact, a temperature sequence amongst the sources, it is useful to compare the dust colour temperatures at different wavelengths. Assuming dust radiates as a blackbody, and using the 45 μm and 100 μm fluxes determined from ISO-LWS, Boogert et al. (2000a) found that sources with hotter dust have a more pronounced ^{13}CO$_2$ wing, which is evidence of processing. Another useful temperature tracer is the CO$_2$ ice abundance. For massive objects with a low CO$_2$ abundance the ^{13}CO$_2$ peak
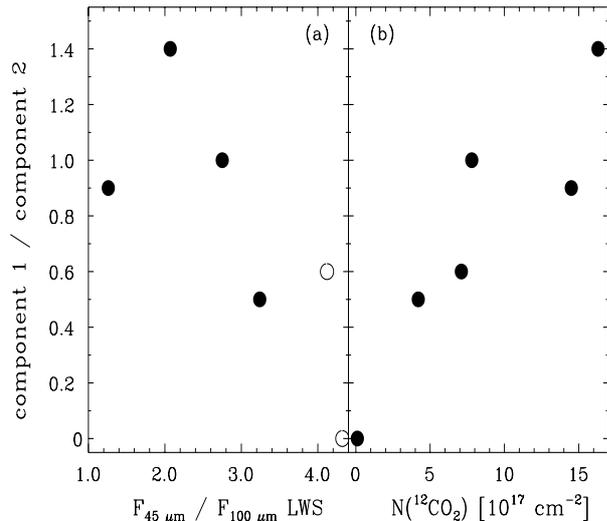
Fig. 14. The ratio of component 1 to component 2 as a function of the ratio of hot to cold dust **a)** and the total CO_2 column density **b)**. Open symbols are for sources with unreliable (contaminated) 45/100 μm flux.

is narrower, evidence for an ice that has been processed. Furthermore, sources displaying a high hot/cold dust ratio also appear to have a larger column of cold CO_2 ice.

Extending this analysis to the 6.85 μm absorption feature reveals a similar trend; that is, the variation in the profile of the 6.85 μm band parallel the trend of thermal processing obvious from these tracers. Sources which display a large amount of component 2 in the 6.85 μm band also have a high hot/cold dust flux ratio (Table 2; Fig. 14a). As the amount of component 2 contributing to the 6.85 μm band decreases so too does the amount of hot dust. Similarly, comparing the ratio of the components contributing to the 6.85 μm band and the CO_2 column density reveals that sources with a greater amount of component 1 also show have a larger CO_2 column densities (Fig. 14b) indicating that these are colder sources. Decreasing contribution of component 1 correlates with decreasing abundance of CO_2, demonstrating that our sources also display a temperature (evolution) trend as noted by others (Boogert 1999; Boogert et al. 2000a; Gerakines et al. 1999). Because it is unlikely that there are two (unknown) species which have dominant absorption bands near 6.85 μm and no other obvious bands, we conclude that upon thermal processing, the peak position of the "6.85 μm" interstellar band shifts from about 6.85 μm to 7.0 μm.

## 6.2. Composition and chemistry of interstellar ices

Comparison of the interstellar spectra, along different lines of sight, provides a more complete inventory of the ice mantles. The pivotal reactions which govern the composition of interstellar ices arise from the hydrogenation and oxidation of CO. In recognition of the recent ISO observations, it is timely to reconsider the chemical origin of the

detected molecules and to compare the observed abundances with theoretical models.

Table 3 summarizes the observed composition of interstellar ices towards deeply embedded objects. The most striking aspect of this table is the apparent simplicity of the composition of interstellar ices. Infrared observations clearly show that interstellar grain mantles consist mainly of H_2O, as evidenced by the strength of the 3.1 μm and 6.0 μm H_2O ice bands. In the majority lines of sight, CO_2 is the second most abundant molecule, except toward GL 7009S where CH_3OH is the second most abundant molecule.

It is generally accepted that grain surface reactions, through hydrogenation and oxidation of accreting species, favours the formation of simple molecular species (Tielens & Hagen 1982; Hasegawa & Herbst 1993; Hiraoka et al. 1994). The composition of the grain mantle is determined by the most abundant accreting species. H_2O ice is observed to be the dominant component of grain mantles, but the mechanism for forming H_2O is somewhat uncertain. H_2O might be formed through direct reactions of accreted O and H atoms. However, in a diffusion limited grain surface network, there will never be an H "waiting" for an O to initiate the H_2O formation, since H reacts readily with CO and other species (or evaporates; Tielens & Charnley 1997). The fate of an accreted O is less certain. Some studies (Tielens & Hagen 1982) suggest O reacts rapidly (i.e. on timescales of a day) with CO and, hence, the direct H_2O formation route from O + H is also blocked. If O were to react with CO, then H_2O formation has to occur through O_2 and O_3 hydrogenation (where O_3 is formed from O_2 + O) and theoretical calculations show that this is a major route (Tielens & Hagen 1982). However, other studies maintain that the O + CO reaction does not occur (Grim & d'Hendecourt 1986), leaving the O available for H_2O formation.

CO is directly accreted from the gas phase. The reaction pathway to H_2CO and CH_3OH is through the sequential addition of H:

$$CO \rightarrow HCO \rightarrow H_2CO \rightarrow CH_2OH \rightarrow CH_3OH. \quad (1)$$
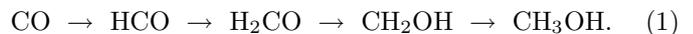
The reaction proceeds relatively unhindered through the ability of H to tunnel through any activation barriers and react with a species on the grain surface. The intermediate radical, HCO, can rapidly react with other atoms including O which can lead to HCOOH formation. The reactions involved have been studied in the laboratory by van Ijzendoorn et al. (1983), and more recently by Hiraoka et al. (1994, 1998). These studies seem to imply that H_2CO is more susceptible to hydrogenation than CO. Indeed, the probability for the reaction of an accreted H atom with an H_2CO molecule is 10^3 times more likely than with a CO molecule. Using these relative probabilities the abundance ratios of CO, H_2CO and CH_3OH can be readily calculated (Charnley et al. 1997). In this scheme, the relative abundances of CO, H_2CO, and CH_3OH will depend on the ratio of the H and CO accretion rates, α_H, and the quantity $\phi_H = Prob\{CO\}/Prob\{H_2CO\}$, where $Prob\{X\}$

Table 2. Column densities[a], observed physical parameters and the ratio of the 2 components seen along different lines of sight.

Object	$\frac{C1}{C2}$[b]	H$_2$O		HCOOH	H$_2$CO	CO$_2$	$\frac{F_{hot}}{F_{cold}}$[c]	T_{H_2O}	$T_{hotcore}$	Ref
		3.1 μm	6 μm					K	K	
NGC 7538:IRS9	1.4	70	100	1.8	3.1	16.3	2.1	10	180 $\pm$ 40	1, 2, 1, 1, 3, 4, 1, 5
GL 7009S	1	-	110	-	3.3	25	1.0	10	740 $\pm$ 255	1, 6, 7, 6, 1, 1, 8
W 33A	0.9	110	400	1.8	7.1	14.5	1.3	10	120 $\pm$ 14	1, 9, 1, 1, 1, 3, 4, 1, 5
GL 989	1.3	20	46	0.4	0.6	-	-	10	-	1, 10, 1, 1, 1, 1
GL 2136	1.0	50	57	1.0	1.6	7.8	2.8	$\leq$30	580 $\pm$ 60	1, 11, 1, 1, 3, 4, 1, 5
Elias 29	1	30	60	-	-	6.48	2.0	$\leq$50	1100 $\pm$ 300	1, 12, 1, 12, 4, 1, 4
S 140:IRS1	0.5	20	56	-	-	4.2	3.2	10	390 $\pm$ 10	1, 2, 1, 3, 4, 1, 5
W 3:IRS5	0.6	58	63	-	-	7.1	4.1	10	577 $\pm$ 10	1, 2, 1, 3, 4, 1, 5
Mon R2:IRS3	0.0	16	59	-	-	0.1	4.3	80	310 $\pm$ 34	1, 10, 1, 13, 4, 1, 14
HH 100	1	24	57	-	-	5.9	1.1	10	-	1, 15, 1, 14, 4, 1

[a] In units of 10^{17} cm^{-2}; [b] ratio of component 1 to component 2; [c] calculated as $F(45\ \mu m)/F(100\ \mu m)$ from ISO-LWS spectra.
References: (1) This work; (2) Allamandola et al. (1992); (3) Gerakines et al. (1999); (4) Boogert et al. (2000a); (5) Mitchell et al. (1990); (6) d'Hendecourt et al. (1996); (7) d'Hendecourt et al. (1999); (8) Dartois et al. (1998); (9) Gibb et al. (2000); (10) Smith et al. (1989); (11) Skinner et al. (1992); (12) Boogert et al. (2000b); (13) Boogert (private communication); (14) Giannakopoulou et al. (1997); (15) Whittet et al. (1996).

Table 3. Relative abundances of ice species detected towards different lines of sight compared with predicted abundances from theoretical models[a].

Ice	NGC 7538 IRS9	GL 7009S	W 33A	GL 989	GL 2136	Elias 29	S 140 IRS1	W 3 IRS5	Mon R2 IRS3	HH100	Theory[b]
H$_2$O	100	100	100	100	100	100	100	100	100	100	100
CO	12	15	2.2	5.2	1.9	3	0.4	2.5	-	11.7	0.4
CO$_2$	16.3	21	3.6	-	13	10.8	7.5	11.3	0.17	5.8	9
CH$_3$OH	3.2	30	5	-	4.5	2	6.8	8.4	1.5	-	43
CH$_4$	1.3	3.6	0.4	-	-	0.8	-	-	-	-	0.007[c]
HCOOH	$\lesssim$3	-	$\lesssim$3	1	1.7	-	-	-	-	-	0.003
H$_2$CO	2	3	2	1.3	3	-	-	-	-	-	-[d]
OCS	-	0.17	0.05	0.04	-	0.04	-	-	-	-	0.4
NH$_3$	9.3	-	4.5	-	-	4.6	-	-	-	4.2	1
XCN[e]	0.9	3.7	2	-	0.3	0.1	-	-	-	-	-
CO(apolar)	11.6	-	0.5	1.5	-	2.4	-	1.7	-	7.9	-
: No match $\frac{N(H_2O)\ 3\ \mu m}{N(H_2O)\ 6\ \mu m}$[f]	1.4	-	3.6	2.1	1.1	2.4	2.8	1.1	3.5	2	
Notes[g]	1	2	3	4	5	6	7	8	9	10	

[a] All results are expressed as a percentage of the 6.0 μm $N(H_2O)$ column density; [b] determined under the reducing condition of $n = 10^4$ cm^{-3}; [c] CH$_4$ is formed through hydrogenation of atomic C, which was underestimated in these calculations (see text); [d] The Tielens & Hagen calculations stopped hydrogenation of CO at H$_2$CO. Recent experimental and theoretical studies (Hiraoka et al. 1994; Charnely et al. 1997) show that with H-rich conditions, essentially all H$_2$CO is converted into CH$_3$OH; [e] assuming that the band is OCN$^-$; [f] multiply the abundance by this ratio to compute the abundance relative to the 3.1 μm $N(H_2O)$ column density; [g] notes: (1) Data from Boogert et al. (1996); Chiar et al. (1996); Demyk et al. (1998); Gerakines et al. (1999); this work; (2) data from Dartois et al. (1998); Dartois et al. (1999); (3) data from Boogert et al. (1996); Chiar et al. (1996); Demyk et al. (1998); Gerakines et al. (1999); Gibb et al. (2000); this work; (4) data from Boogert (private communication); Palumbo et al. (1997); (5) data from Brooke et al. (1999); Gerakines et al. (1999); Pendleton et al. (1999); Schutte et al. (1996); (6) data from Boogert et al. (2000b); (7) data from Allamandola et al. (1992); Gerakines et al. (1999); (8) data from Allamandola et al. (1992); Gerakines et al. (1999); (9) data from Boogert (private communication); Smith et al. (1992); (10) data from Boogert et al. (2000a); Whittet et al. (1996).

is the probability for a single H on a grain surface to react with a single X; i.e., ϕ_H represents the competition between CO and H$_2$CO for atomic H. In Fig. 15 we compare our observed values with the theoretical abundance ratios of CO/CH$_3$OH and H$_2$CO/CH$_3$OH for different values of ϕ_H (solid lines). For comparison, the abundance ratios of the warm gas observed in the compact ridge of Orion, which are generally supposed to originate from evaporated
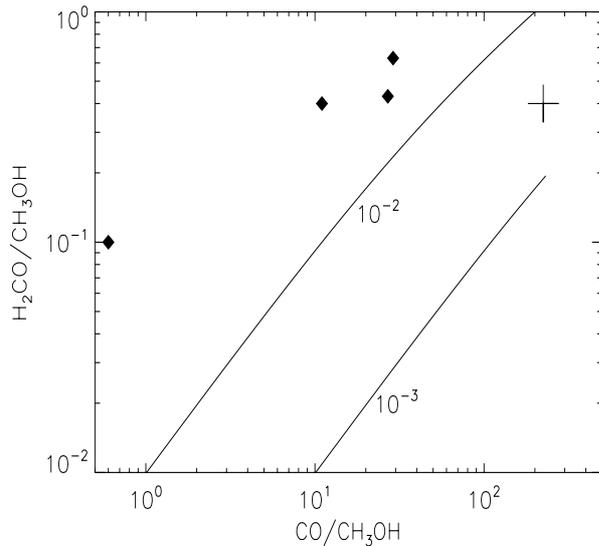
Fig. 15. Measured abundance ratios of H_2CO and CO relative to CH_3OH in interstellar ices (diamonds). The solid lines represents the model results from the hydrogenation of CO (cf. text for details; Charnley et al. 1997). Along the curve, the CO/H accretion probability varies from small (left) to large (right). The cross indicates observed abundances in the Orion Compact Ridge (Wright et al. 1996).

ices, are also shown. The agreement between observations and models lends general support to the proposed hydrogenation scheme of CO on grain surfaces as the origin of CH_3OH and H_2CO in interstellar ices, if H/CO $\sim 10^{-2}$.

Grain surface reactions can form HCOOH through the reactions of accreted atomic oxygen with the formyl radical, HCO, produced through the hydrogenation of CO. The observed $HCOOH/H_2O$ abundance ratio is in agreement with calculations at low gas phase densities ($\sim 10^{-3}$ cm^{-3}; Tielens & Hagen 1982).

As discussed above, grain surface chemistry may also lead to the formation of CO_2 if the reaction of atomic O with CO is rapid. Calculated abundances ($CO_2/H_2O \sim 0.1$, independent of density) agree well with the observations. However, if the reaction were instead slow, then CO_2 might be formed through photolysis, likely of ices containing H_2O and CO (Whittet et al. 1998). The relatively constant CO_2/H_2O ratio in interstellar ices suggests that photolysis is unlikely to be important.

Likewise, CH_4 can be formed through hydrogenation of accreted C atoms. Earlier grain chemistry models, (Tielens & Hagen 1982), had little gaseous C and consequently predicted little CH_4 to be present in the ice. Currently, it is generally accepted that UV photons produced by cosmic ray excitation of H_2 (Prasad & Tarafdar 1983) keep about 1% of the carbon in atomic form (Gredel et al. 1989) in the gas phase and this can explain the measured solid CH_4 abundances. Those grain chemistry models which start from a fully atomic gas produce copious amounts of solid CH_4 (d'Hendecourt & Allamandola 1986; Brown et al. 1988) which is not observed and this scenario can therefore be ruled out (Boogert et al. 1998).

The synthesis of NH_3 is through the hydrogenation of N on interstellar grain surfaces. Most of the nitrogen in the gas phase may be locked up in N_2 and hence the abundance of NH_3 in grain surface models is generally low. The low abundance of solid NH_3 in interstellar ices again implies grain surface chemistry starting from an accreting molecular gas. Finally, OCS is thought to form through the reaction O + CS (Tielens & Hagen 1982) which has a negligible activation barrier (Palumbo et al. 1997).

An alternative way to produce some of these simple molecules is by various forms of processing. Ultra-violet photolysis of CO containing ices has been suggested as an alternative way to form interstellar CO_2 (see above). The UV photons generate small radicals which, because of the excess energy available, can overcome considerable activation barriers. In particular, UV photolysis of CO and NH_3 mixtures has been suggested as a possible mechanism for the production of the XCN feature (Grim & Greenberg 1987; Schutte & Greenberg 1997). However, recent laboratory studies have shown that the XCN band can also be produced by acid-base reactions of HNCO and NH_3 (Keane 1997; Keane et al. in prep.). Though laboratory experiments also indicate that UV photolysis can lead to rather complex molecules, there is a lack of observational evidence for their presence. Summarizing, except for the 4.62 μm XCN band and possibly the unidentified 6.85 μm band, all observed features are due to simple molecules whose abundances may be well explained by simple grain surface reactions.

7. Summary and conclusions

We have observed the 5–8 μm region toward a sample of 10 protostars. The observations clearly show that both the 6.0 μm and 6.85 μm absorption feature, detected toward all sources, vary in position, width and relative intensity. The bulk of the 6.0 μm feature is H_2O ice and, for three of the sources, appears to be the only component contributing to this band. For the remaining sources additional components are absorbing in the 6.0 μm band. It seems clear that there are at least 3 additional components present in the 6.0 μm band. The extra absorption has been attributed to HCOOH (at 5.83 μm), H_2CO (at 5.81 μm) and aromatic structures (at 6.2 μm). A fourth component, NH_3, is also believed to be contributing to the absorption but is not readily detected due to the strength of the H_2O ice band.

The H_2O column density derived from the 6.0 μm feature is, for all sources, consistently greater than the column density derived from the 3.1 μm band. However, if the long wavelength wing of the 3.1 μm band is attributed to absorption by H_2O ice, the 6.0 μm and 3.1 μm column densities are more consistent with each other. All sources are best fitted by a cold ($T \leq 50$ K) laboratory amorphous H_2O ice, except Mon R2:IRS3 which is fitted by an 80 K profile, which is consistent with previous work (Smith et al. 1989).

The 6.85 μm band displays systematic variations in position and profile, which we attribute to two components based upon the two extremes of peak position (NGC 7538:IRS9 and Mon R2:IRS3) seen along the different lines of sight. The 6.85 μm features of all sources can be fitted by varying combinations of these components. Furthermore, there is a notable trend in the data which shows that the shift in 6.85 μm peak position parallels the lack of additional components contributing to the 6.0 μm band and hence may be attributed to thermal processing of ices. The 6.85 μm band in those sources with warmer ice and dust are comprised mainly of the Mon R2:IRS3 profile.

No satisfactory candidate for the 6.85 μm band has been found. CH_3OH, long believed to be the carrier of this band, can contribute at most only a small fraction to the band, based on the abundance determined from the 3.54 μm CH_3OH feature. The strong triple peak structure observed in laboratory CH_3OH spectra is also not seen in the interstellar 6.85 μm band. Contribution from NH_4^+ is minimal, based on the abundance of counter ions. Furthermore, the 6.85 μm feature does not seem to correlate with absorption bands of other ions. Finally, an assignment to carbonates is not realistic, since the profiles of the carbonate features are considerably broader than the interstellar 6.85 μm band.

References

Allamandola, L. J., Sandford, S. A., Tielens, A. G. G. M., & Herbst, T. M. 1992, ApJ, 399, 134

Boogert, A. C. A., Helmich, F. P., van Dishoeck, E. F., et al. 1998, A&A, 336, 352

Boogert, A. C. A. 1999, Ph.D. Thesis, University of Groningen

Boogert, A. C. A., Ehrenfreund, P., Gerakines, P. A., et al. 2000a, A&A, 353, 339

Boogert, A. C. A., Tielens, A. G. G. M., Ceccarelli, C., et al. 2000b, A&A, 360, 683

Boonman, A. M. S., van Dishoeck, E. F., Lahuis, F., Wright, C. M., & Doty, S. D. 2000, in ISO beyond the Peaks, ESA SP-456, 67

Brooke, T. Y., Sellgren, K., & Smith, R. G. 1996, ApJ, 459, 209

Brooke, T. Y., Sellgren, K., & Geballe, T. R. 1999, ApJ, 517, 883

Brown, P. D., Charnley, S. B., & Millar, T. J. 1988, MNRAS, 231, 409

Brucato, J. R., Palumbo, M. E., & Strazzula, G. 1997, Icarus, 125, 135

Charnley, S. B., Tielens, A. G. G. M., & Rodgers, S. D. 1997, ApJ, 482, L203

Chiar, J. E., Tielens, A. G. M. M., Whittet, D. C. B., et al. 2000, ApJ, 537, 749

Colangeli, L., Mennella, V., Palumbo, P., Rotundi, A., & Bussoletti, E. 1995, A&AS, 113, 561

Dartois, E., d'Hendecourt, L., Boulanger, F., et al. 1998, A&A, 331, 651

Dartois, E., Schutte, W. A., Geballe, T. R., et al. 1999, A&A, 342, L32

Duley, W. W., & Williams, D. A. 1981, MNRAS, 196, 296

Gerakines, P. A., Whittet, D. C. B., Ehrenfreund, P., et al. 1999, ApJ, 522, 357

Giannakopoulou, J., Mitchell, G. F., Hasegawa, T. I., Matthews, H. E., & Maillard, J. P. 1997, ApJ, 487, 346

de Graauw, Th., Haser, L. N., Beintema, D. A., et al. 1996, A&A, 315, L49

Gibb, E. L., Whittet, D. C. B., Schutte, W. A., et al. 2000, ApJ, 536, 347

Gredel, R., Lepp, S., Dalagarno, A., & Herbst, E. 1989, ApJ, 347, 289

Grim, R. J. A., & d'Hendecourt, L. B. 1986, A&A, 167, 161

Grim, R. J. A., Greenberg, J. M., de Groot, M. S., et al. 1989, A&A, 78, 161

Grim, R. J. A., Bass, F., Greenberg, J. M., Geballe, T. R., & Schutte, W. A. 1991, A&A, 243, 473

Hagen, W., Tielens, A. G. G. M., & Greenberg, J. M. 1980, ApJ, 86, L3

Hagen, W., Tielens, A. G. G. M., & Greenberg, J. M. 1981, J. Chem. Phys., 56, 367

Hagen, W., Tielens, A. G. G. M., & Greenberg, J. M. 1983, A&AS, 51, 389

Hasegawa, T. I., & Herbst, E. 1993, MNRAS, 261, 83

Hecht, J. H., Russell, R. W., Stephens, J. R., & Grieve, P. R. 1986, ApJ, 309, 90

Helmich, F. P., van Dishoeck, E. F., Black, J. H., et al. 1996, A&A, 315, L173

d'Hendecourt, L. B., & Allamandola, L. J. 1986, A&AS, 64, 453

d'Hendecourt, L. B., Jourdain de Muizon, M., & Dartois, E. 1996, A&A, 315, L365

d'Hendecourt, L. B., Jourdain de Muizon, M., Dartois, E., et al. 1999, Proceedings The Universe as seen by ISO, ed. P. Cox, & M. F. Kessler, ESA Publications, 589

Hiraoka, K., Ohashi, N., Kihara, Y., et al. 1994, Chem. Phys. Lett., 229, 408

Hiraoka, K., Miyagoshi, T., Takayama, T., Yamamoto, K., & Kihara, Y. 1998, ApJ, 498, 710

Huang, C. K., & Kerr, P. F. 1960, J. Mat. Mineral, 45, 311

Hudgins, D. M., & Allamandola, L. J. 1995, J. Chem. Phys., 99, 3033

Hudgins, D. M., Sandford, S. A., Allamandola, L. J., & Tielens, A. G. G. M. 1993, ApJS, 86, 713

Huffmann, D. R. 1977, Adv. Phys., 26, 129

Keane, J. V. 1997, Masters Thesis, Leiden University

Lacy, J. H., Faraji, H., Sandford, S. A., & Allamandola, L. J. 1998, ApJ, 501, L105

Langhoff, S. R. 1996, J. Phys. Chem., 100, 2819

Lepp, S., & Dalgarno, A. 1988, ApJ, 325, 553

Léger, A., Grauthier, S., Défourneau, D., & Rouan, D. 1983, A&A, 117, 164

Maldoni, M. M., Smith, R. G., Robinson, G., & Rookyard, V. L. 1998, MNRAS, 298, 251

Maréchal, Y. 1987, J. Chem. Phys., 87, 6344

Mathis, J. S., Mezger, P. G., & Panagia, N. 1983, A&A, 128, 212

Merril, K. M., Russel, R. W., & Soifer, B. T. 1976, ApJ, 207, 763

Moore, M. H., & Khanna, R. K. 1991, Spectrochim. Acta, 47, 255

Palumbo, M. E., Geballe, T. R., & Tielens, A. G. G. M. 1997, ApJ, 479, 839

Pendleton, Y. J., Tielens, A. G. G. M., & Werner, M. W. 1990, ApJ, 349, 107

Prasad, S., & Tarafdar, S. P. 1983, ApJ, 267, 603

Sandford, S. A., & Walker, R. M. 1985, ApJ, 291, 838

Schutte, W. A., Allamandola, L. J., & Sandford, S. A. 1993, Icarus, 104, 118

Schutte, W. A., Tielens, A. G. G. M., Whittet, D. C. B., et al. 1996, A&A, 315, L333

Schutte, W. A., & Greenberg, J. M. 1997, A&A, 317, L43

Schutte, W. A., Van der Hucht, K. A., Whittet, D. C. B., et al. 1998, A&A, 337, 261

Schutte, W. A., Boogert, A. C. A., Tielens, A. G. G. M., et al. 1999, A&A, 343, 966

Sellgren, K., Smith, R. G., & Brooke, T. Y. 1994, ApJ, 433, 179

Sellgren, K., Brooke, T. Y., Smith, R. G., & Geballe, T. R. 1995, ApJ, 449, L69

Smith, R. G., Sellgren, K., & Tokunaga, A. T. 1989, ApJ, 382, 523

Tielens, A. G. G. M. 1989, in Interstellar Dust, ed. L. J. Allamandola, & A. G. G. M. Tielens (Kluwer, Dordrecht), 239

Tielens, A. G. G. M., & Hagen, W. 1982, A&A, 114, 245

Tielens, A. G. G. M., Allamandola, L. J., Bregman, J., et al. 1984, ApJ, 287, 697

Tielens, A. G. G. M., & Allamandola, L. J. 1987, in Physical Processes in Interstellar Clouds, ed. G. E. Morfill, & M. Scholer, 333

Tielens, A. G. G. M., & Charnley, S. B. 1997, in Origin of Life and Evolution of the Biosphere, 27, 23

Tielens, A. G. G. M., Hony, S., van Kerckhoven, C., & Peeters, E. 1999, Proceedings The Universe as seen by ISO, ed. P. Cox, & M. F. Kessler, ESA Publications, 579

van Dishoeck, E. F., & Helmich, F. P. 1996, A&A, 315, L177

van Ijzendoorn, L., Allamandola, L. J., Bass, F., & Greenberg, J. M. 1983, J. Chem. Phys., 78, 7019

Whittet, D. C. B. 1993, in Dust and Chemistry in Astronomy, ed. T. J. Millar, & D. A. Williams (Institute of Physics, Bristol), 9

Whittet, D. C. B., Schutte, W. A., Tielens, A. G. G. M., et al. 1996, A&A, 315, L357

Whittet, D. C. B., Gerakines, P. A., Tielens, A. G. G. M., et al. 1998, ApJ, 498, L159

Wexler, A. S. 1967, Appl. Spec. Rev., 1, 29

Willner, S. P., Gilletet, F. C., Herter, T. L., et al. 1982, ApJ, 253, 174

Wright, M. C. H., Plambeck, R. L., & Wilner, D. J. 1996, ApJ, 469, 216